ARTICLE   OPEN

Check for updates

Fire carbon emissions over Equatorial Asia reduced by shortened dry seasons

Sifan Wang[1], Bin He [1]✉, Hans W. Chen [2], Deliang Chen [3], Yaning Chen [4], Wenping Yuan [5], Feng Shi [6], Jianping Duan[7], Wei Wu[8], Tiexi Chen[9,10], Lanlan Guo[1], Ziqian Zhong [1], Weili Duan [4], Zhi Li[4], Weiguo Jiang[1], Ling Huang[11], Xingming Hao[4,12], Rui Tang[1], Huiming Liu[13], Yafeng Zhang[1] and Xiaoming Xie[1]

Fire carbon emissions over Equatorial Asia (EQAS) play a critical role in the global carbon cycle. Most regional fire emissions (89.0%) occur in the dry season, but how changes in the dry-season length affect the fire emissions remains poorly understood. Here we show that, the length of the EQAS dry season has decreased significantly during 1979–2021, and the delayed dry season onset (5.4 ± 1.6 (± one standard error) days decade^{-1}) due to increased precipitation (36.4 ± 9.1 mm decade^{-1}) in the early dry season is the main reason. The dry season length is strongly correlated with the length of the fire season. Increased precipitation during the early dry season led to a significant reduction (May: -0.7 ± 0.4 Tg C decade^{-1}; August: -12.9 ± 6.7 Tg C decade^{-1}) in fire carbon emissions during the early and peak fire season. Climate models from the Coupled Model Intercomparison Project Phase 6 project a continued decline in future dry season length in EQAS under medium and high-emission scenarios, implying further reductions in fire carbon emissions.

INTRODUCTION

Equatorial Asia (EQAS) contains one of the largest tropical rainforest areas and is a major carbon pool (Supplementary Fig. 1a, b)[1], but increasing human disturbance is converting the region from a carbon sink to a source, especially with fire carbon emissions from peat burning and deforestation[2]. Fires in EQAS occur mainly on peatlands, which store about 70 Pg of organic carbon[3]. During the extreme drought of 1997, carbon released through peatland fires was estimated to be equivalent to 13–40% of the mean annual global carbon emissions from fossil fuels at the time[4]. Despite most fires resulting from human activities, their interannual variation is strongly regulated by precipitation changes associated with large-scale climatic fluctuations[5–7]. During El Niño years, for example, abnormal precipitation deficits in the dry season are associated with severe fires and high carbon emissions[8,9]. The Indian Ocean dipole also affects drought conditions in the region and thus fire carbon emissions[10]. A better understanding of the influence of climatic drivers on fire emissions over EQAS is thus critical for accurately projecting the future carbon cycle and budget.

Climate changes in the dry season over rainforest regions have aroused great concerns owing to their impact on ecosystems and regional carbon cycles[11–13]. In the Amazon and Congo rainforests, precipitation decreases have increased dry season length (DSL) over the recent decades[11–13]. In the Amazon, the delayed ending of the dry season has increased the risk of fires and prolonged the fire season[11]. Whether precipitation and the associated DSL have

changed over EQAS is unclear. Fires in EQAS usually break out during the dry season (Supplementary Fig. 1c, d)[14], and previous studies have reported a nonlinear negative response of fire carbon emissions to dry season precipitation[14,15]. However, how changes in the DSL impact fire emissions remains unknown.

In this study, changes in precipitation and DSL in EQAS were examined using multiple precipitation datasets during 1979–2021, and their relationships with fire activities and fire emissions were explored based on active fire counts from the Terra Moderate Resolution Imaging Spectroradiometer (MODIS) Thermal Anomalies and Fire Eight-Day (MOD14A2)[16] data, the monthly Global Fire Emissions Database v. 4.1 (GFED4s)[17], and long-term daily airport visibility records. Future precipitation and DSL changes and the reasons for historical and future precipitation increases were investigated through model projections from the Coupled Model Intercomparison Project Phase 6 (CMIP6)[18].

RESULTS AND DISCUSSION

Increased precipitation and shortened dry seasons

Mean annual precipitation over EQAS increased during 1979–2021 (Supplementary Fig. 2a). Significant precipitation increases were found in the precipitation datasets from the Climate Prediction Center Unified Gauge-Based Analysis of Global Daily Precipitation (CPC-U)[19] and the European Centre for Medium-Range Weather Forecasts (ECMWF) Reanalysis v. 5 (ERA5)[20], with trends of 127.5 ± 35.8 mm decade^{-1} ($p = 0.002$) and 100.6 ± 33.8 mm

[1]State Key Laboratory of Earth Surface Processes and Resource Ecology, Faculty of Geographical Science, Beijing Normal University, Beijing 100875, China. [2]Department of Physical Geography and Ecosystem Science, Lund University, Lund S-22362, Sweden. [3]Regional Climate Group, Department of Earth Sciences, University of Gothenburg, Gothenburg S-40530, Sweden. [4]State Key Laboratory of Desert and Oasis Ecology, Xinjiang Institute of Ecology and Geography, Chinese Academy of Sciences, Urumqi 830011, China. [5]School of Atmospheric Sciences, Sun Yat-Sen University, Guangzhou 510275, China. [6]Key Laboratory of Cenozoic Geology and Environment, Institute of Geology and Geophysics, Chinese Academy of Sciences, Beijing 100029, China. [7]CAS Key Laboratory of Regional Climate-Environment for Temperate East Asia, Institute of Atmospheric Physics, Chinese Academy of Sciences, Beijing 100029, China. [8]National Disaster Reduction Center of China, Ministry of Emergency Management, Beijing 100124, China. [9]Collaborative Innovation Center on Forecast and Evaluation of Meteorological Disaster, School of Geographical Sciences, Nanjing University of Information Science and Technology, Nanjing 210044, China. [10]School of Geographical Sciences, Qinghai Normal University, Xining 810008, China. [11]College of Urban and Environmental Sciences, Peking University, Beijing 100871, China. [12]Akesu National Station of Observation and Research for Oasis Agro-ecosystem, Akesu 843017 Xinjiang, China. [13]Ministry of Ecology and Environment Center for Satellite Application on Ecology and Environment, Beijing 100094, China. ✉email: hebin@bnu.edu.cn

npj

decade^{-1} ($p = 0.020$) during 1979–2021, respectively. Although there has been no significant upward trend in the precipitation from the Global Precipitation Climatology Project (GPCP)[21] dataset during 1979–2016, a significant ($p = 0.036$) turning point in precipitation trend was identified in 1991 (Supplementary Fig. 2a), and there is a significant positive precipitation trend during 1991–2016 with a rate of 168.1 ± 75.4 mm decade^{-1} ($p = 0.036$). In general, increased precipitation has been observed over most of EQAS for all months during 1979–2021, especially for April–June and November–December (Supplementary Fig. 2b–d). Negative precipitation trends have been observed for only a small region in southwest Sumatra (Supplementary Fig. 2b–d). As an independent evidence of increased precipitation over EQAS, the terrestrial water storage (TWS) retrieved from the Gravity Recovery and Climate Experiment (GRACE) has also had a significant positive trend since 2003 (Supplementary Fig. 3). To decide which precipitation product to use in the further analysis, we calculated the correlations between annual precipitation from the different products and the TWS. Relatively strong correlations were observed between the TWS and the CPC-U product, compared with the ERA5 and GPCP. Therefore, we used the CPC-U precipitation product for the following analysis (Supplementary Table 1).

Associated with increased precipitation, the EQAS DSL shows a significant negative trend during 1979–2021 in the CPC-U dataset, with a rate of -10.2 ± 3.5 d decade^{-1} ($p = 0.001$) (Fig. 1a). The shortening of DSL was caused by a larger delay in dry season onset (DSO) (5.4 ± 1.6 d decade^{-1}, $p = 0.002$; Fig. 1b) than the advancement of dry season end (DSE) (4.7 ± 2.2 d decade^{-1}, $p = 0.037$; Fig. 1c). During the transition period from rainy to dry season (April–June, AMJ), precipitation increased significantly between 1979 to 2021 by 33.7 ± 8.9 mm decade^{-1} ($p = 0.001$) in CPC-U (Fig. 1d), resulting in a significant delay in DSO. Spatially, the decrease in DSL was extensive in EQAS (Fig. 1e). Regions with significantly reduced DSL ($p < 0.1$) were distributed mainly in northern Sumatra, Kalimantan, Sulawesi, and New Guinea (Fig. 1e). Areas with the largest DSL changes generally experienced large delays in DSO (increased precipitation in AMJ) or advancements in DSE (Fig. 1f-h). The spatial features of dry season changes derived from the other precipitation products are generally consistent with the CPC-U patterns for EQAS (Supplementary Fig. 4).

Regarding the increase in precipitation in EQAS, previous studies have shown a strong correlation between precipitation in EQAS and the surrounding sea surface temperature[22]. Due to the increase of atmospheric carbon dioxide (CO_2), the western Pacific Ocean has warmed more than the central Pacific Ocean, further strengthening the zonal SST gradient[23] and thus enhancing the trade winds and the Walker circulation[24], promoting the transport of ocean currents and warm, moist air towards EQAS, and also helping to increase local precipitation.

To explore the impact of anthropogenic activities on precipitation and DSL in EQAS, we utilized the hist-nat, hist-aer, and hist-GHG experiments from the CMIP6 models' Detection and Attribution Model Intercomparison Project (DAMIP) simulations[25] to simulate precipitation in EQAS from 1979 to 2020 (Supplementary Table 3) and analyzed the separate responses of precipitation to anthropogenic aerosols and greenhouse gases (GHG)[26]. In order to improve the robustness of our results, we selected 4 from the 12 models that can reproduce the DSL shortening over the historical period (see "Methods"), and show the results of multi-model averaging. As shown in Supplementary Fig. 5, the increase in anthropogenic aerosol emissions has a suppressing effect on precipitation, while the increase in GHG emissions has a promoting effect (Supplementary Fig. 5a–c). From a monthly perspective, the increase in anthropogenic aerosol and GHG emissions mainly affects precipitation during the rainy season in EQAS (Supplementary Fig. 5d). Due to the increase in GHG emissions, the tropical Pacific sea surface temperature gradient is

strengthened, leading to an increase in precipitation in EQAS[23]. Therefore, the increase in EQAS precipitation during the historical period can be attributed to the increase in GHG emissions.

Changes in dry season length regulate fire season length

Precipitation changes and associated dry season changes are expected to impact fire activities and carbon emissions in EQAS[2,14]. To explore how dry season changes have impacted fire activities, we calculated fire seasons using 8-day fire counts during 2001–2021 (see "Methods"). As shown in Fig. 2, as precipitation decreased toward the seasonal minimum in early August, the fire counts increased rapidly, with the fire season beginning in late July. The fire season peaked during August–October, corresponding to the period with annual minimum precipitation. When precipitation increased to the annual average in November, there were no dry conditions to sustain fire activities. The end date of the fire season in early November was slightly later than the DSE date.

The annual fire season length (FSL) in EQAS has decreased significantly since 2001 (-22.8 ± 10.0 d decade^{-1}, $p = 0.079$). Given that the dry season leads the fire season, and the physical connection between dry conditions and increased fire activity, it is likely that the reduced DSL has led to a shortened fire season (Fig. 2b). To explore how changes in DSL have impacted fire activities and carbon emissions, dry season fire activities and carbon emissions were calculated as the total fire counts and fire carbon emissions from the DSO to DSE, including the months of DSO and DSE. Both fire counts and fire emissions display a nonlinear positive response to DSL, indicating that a longer DSL is associated with more fire counts and higher fire emissions (Fig. 2c, d).

Fire activities and carbon emissions over EQAS are concentrated mainly in southern Sumatra (6°S–0°, 99°–106°E) and southern–central Kalimantan (4°S–0°, 110°–117°E; Supplementary Fig. 1). Dry season fire emissions from these two regions account for 71% of the total EQAS dry season emissions during 2001–2021 (Supplementary Fig. 1). The DSL in southern Sumatra displays a trend of first lengthening and then shortening (20.6 ± 6.5 d decade^{-1}, $p = 0.003$), while the DSL in southern–central Kalimantan has significantly decreased since 1979 (12.7 ± 4.6 d decade^{-1}, $p = 0.008$) (Supplementary Fig. 6). Significant correlations between DSL and FSL were observed in these two regions, with FSLs shortening with the reduction in DSLs ($R = 0.75$, $p < 0.001$; $R = 0.85$, $p < 0.001$) (Supplementary Fig. 8a, e). To verify these findings, we also used visibility records from airports in EQAS as a proxy for fire activities, providing a long-term record since 1992. The visibility was quantified using an extinction coefficient (B_{ext}), where a large B_{ext} value indicates low visibility, which is likely caused by smoke from nearby fire activity. We calculated fire seasons using daily B_{ext} from 1992 to 2021 (see "Methods"). FSLs calculated using B_{ext} are reduced in southern Sumatra and southern–central Kalimantan and are well correlated with DSL (Supplementary Fig. 8). DSLs in southern Sumatra and southern–central Kalimantan also have strong nonlinear relationships with dry season fires and B_{ext} (Supplementary Fig. 7).

A previous study found that the start of the fire season peak in the Mega Rice Project area of central Kalimantan is related to the date of annual minimum precipitation[27]. This phenomenon was observed in both EQAS and southern–central Kalimantan (Supplementary Fig. 9a, g). We also found a strong correlation between May–July precipitation and fire-season onset in EQAS ($R = 0.56$, $p = 0.020$), southern–central Kalimantan ($R = 0.44$, $p = 0.089$), and southern Sumatra ($R = 0.80$, $p < 0.001$), implying a dependence of fire-season onset on the change of early dry season precipitation (Supplementary Fig. 9b, e, h). In addition, the end of the fire season is closely related to the DSE ($R = 0.91$, $p < 0.001$ in EQAS; $R = 0.83$, $p < 0.001$ in southern–central Kalimantan; and $R = 0.70$, $p = 0.004$ in southern Sumatra), suggesting that an earlier DSE
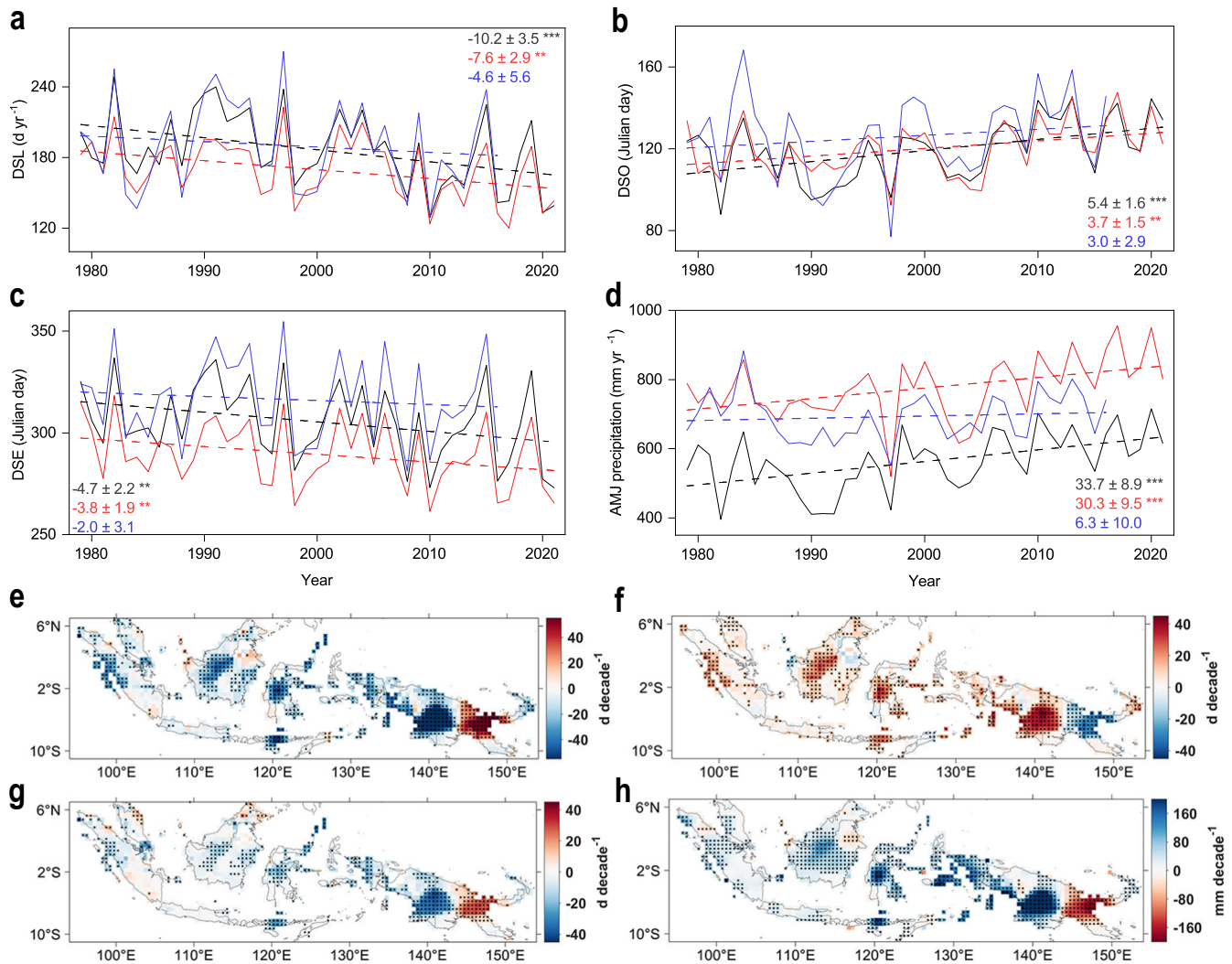
Fig. 1 Dry season changes in Equatorial Asia during 1979–2021. a–d Annual time series and trends in mean dry season length (DSL) (**a**), dry season onset (DSO) (**b**), dry season end (DSE) (**c**), and April–June (AMJ) precipitation (**d**). Because GPCP provides pentad (5-day) precipitation, the 19th to 36th pentads were selected as precipitation for AMJ. Black, red, and blue solid lines indicate the precipitation datasets from CPC-U, ERA5, and GPCP, respectively. The black, red, and blue numbers indicate linear trends (d decade^{-1} or mm decade^{-1}) and standard error for each of the three precipitation datasets, respectively. **e–h** Spatial patterns in linear trends of the DSL (**e**), DSO (**f**), DSE (**g**), and AMJ precipitation (**h**) from CPC-U for 1979–2021. Black dots indicate grids with a significant linear trend ($p < 0.1$). *$p < 0.1$; **$p < 0.05$; ***$p < 0.01$.

usually causes an earlier end of the fire season (Supplementary Fig. 9c, f, i).

Early dry season suppression of fire carbon emissions by increased precipitation

To further explore how precipitation changes have regulated DSL and thereby fire activities and emissions, we analyzed the trends in precipitation, fire carbon emissions, and fire counts month by month in EQAS. To match the time series with fire counts data, we unified the start time of fire emission data to the beginning of the MODIS data (2001–2021). Both fire emissions and counts have decreasing May–October trends in EQAS, with significant decreases being observed in May (-0.7 ± 0.4 Tg C decade^{-1}, $p = 0.077$; and $-0.6 \pm 0.2 \times 10^3$ decade^{-1}, $p = 0.005$, respectively) and August (-12.9 ± 6.7 Tg C decade^{-1}, $p = 0.068$; and $-4.5 \pm 1.7 \times 10^3$ decade^{-1}, $p = 0.016$, respectively) (Fig. 3b, c). Due to the impact of small fires on MODIS-based fire products, there is a certain degree of uncertainty in the results[28,29]. Therefore, we utilized top-down fire CO$_2$ emissions data[30] to

analyze the fire emissions trends in May and August in EQAS, which further confirmed the decreasing trend of fire carbon emissions in EQAS (see "Data uncertainties").

Previous studies indicate that the response of fire carbon emissions to precipitation has a lag of 2–4 months[15,31]. Here, high correlations were found between precipitation in April–May and fire carbon emissions and fire counts in May (Supplementary Fig. 10). Fire carbon emissions and fire counts in August were strongly impacted by May–August precipitation (Fig. 3e, f). This result suggests that increased precipitation in the early dry season suppressed fires in May and August. The TWS retrieved from GRACE was also used here to indicate land water conditions. The TWS shows a 2–4-month lagged response to precipitation (Supplementary Table 2), and a significant upward trend was observed in May–August (Supplementary Fig. 11). This suggests that the increase in precipitation in the early dry season led to an increase in TWS in August, reducing the degree of dryness and leading to a reduction in fire carbon emissions in August (Fig. 3a, g).

Spatially, the reduction in fire carbon emissions was observed mainly in the west and south of Kalimantan and southern Sumatra
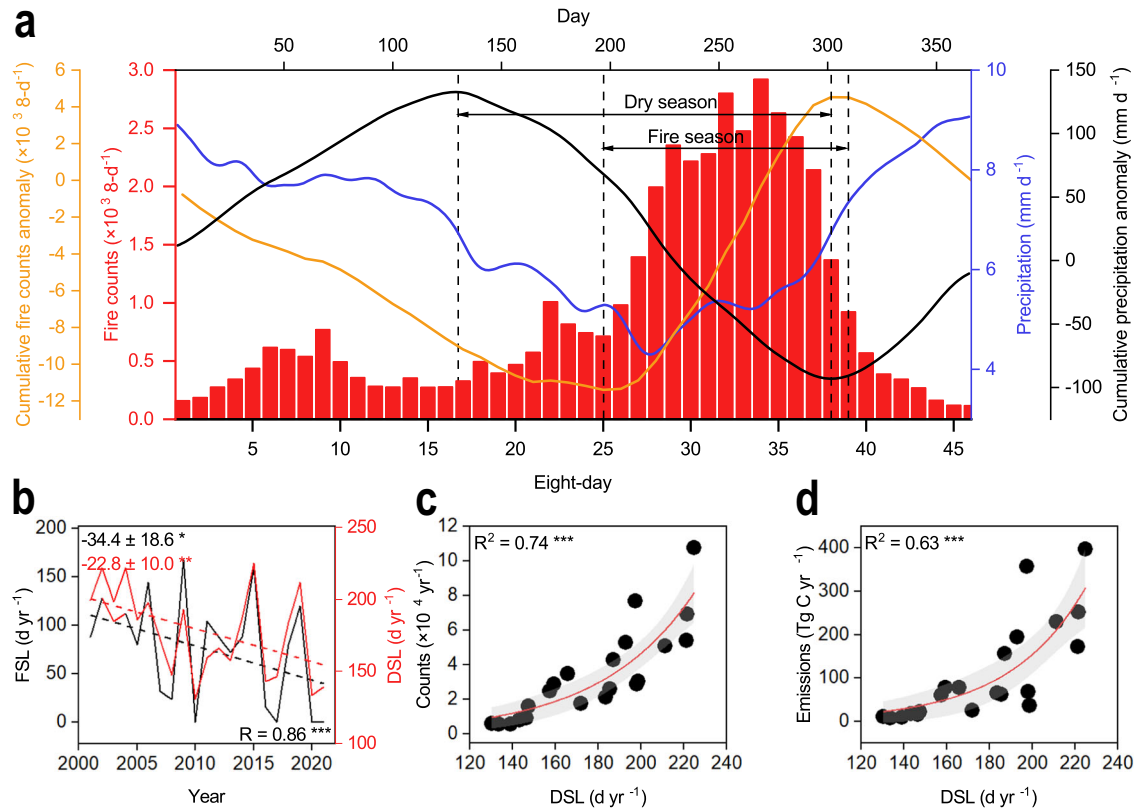
Fig. 2 Relationships between dry season, fire season, and fire activities during 2001–2021. a Relationship between dry and fire seasons, with precipitation and fire counts averaged over 2001–2021. The red bar chart indicates 8-day fire counts, the orange line indicates the cumulative 8-day fire counts anomaly, the blue line indicates the 30-day smoothed daily precipitation, and the black line indicates the 30-day smoothed cumulative daily precipitation anomaly. The inflection points between the black dash line and the cumulative daily precipitation anomaly curve indicate the day of dry season onset (the maximum point of the curve) and end (the minimum point of the curve), and inflection points between the black dash line and the cumulative 8-day fire counts anomaly curve indicate the day of fire season onset (the minimum point of the curve) and end (the maximum point of the curve), respectively. **b** Interannual variations, trends, and correlation between fire-season and dry season lengths. The linear trend (d decade^{-1}) and standard error of DSL and fire season length (FSL) are shown in the top left corners. Correlation coefficients (R) are shown in the lower right corners. **c, d** Exponential fitting of DSL to dry season fire counts (**c**) and fire carbon emissions (**d**). Shading indicates 95% confidence intervals. The coefficient of determination (R^2) is shown in the top left corners. *$p < 0.1$; **$p < 0.05$; ***$p < 0.01$.

(Fig. 3c). The fire carbon emissions and fire counts of the two regions also displayed a downward trend in August, and B_{ext} values decreased from January to August (Supplementary Fig. 12). In both regions, increased precipitation from May to August was found to be associated with decreased fire carbon emissions and counts in August (Supplementary Figs. 11, 13).

Projection of future precipitation and dry season changes
Given the strong association between precipitation, DSL, and fire emissions in EQAS, we investigated projected changes in the first two variables using multi-model ensemble simulations from CMIP6. Daily precipitation data were collected from 20 models (Supplementary Table 3), among which 12 models reproduced the historical shortening trend of DSL from 1979 to 2014 (Supplementary Fig. 14). Accordingly, these 12 models were selected as skillful models for future DSL changes under the four shared socioeconomic pathway (SSP) scenarios: SSP126 (low-emission scenario), SSP245 (medium-emission scenario), SSP370 (medium-emission scenario), and SSP585 (high-emission scenario; see "Methods"). Precipitation averages from the 12 models indicate a continued positive trend from 2023 to 2099, and significant increases in the trends occurred under the SSP245, SSP370, and SSP585 scenarios (Supplementary Fig. 15). In the SSP126 scenario, the multi-model average DSL shows a slight increase, while it decreases in the SSP245, SSP370, and SSP585 scenarios,

particularly in the SSP370 and SSP585 scenarios (-0.8 ± 0.4 d decade^{-1}, $p = 0.038$; and -0.9 ± 0.4 d decade^{-1}, $p = 0.015$, respectively; Fig. 4a). The significant delay in DSO is the main reason for the DSL reduction in the SSP370 and SSP585 scenarios (Fig. 4b). DSE was advanced in all four scenarios, but only significantly in the SSP245 scenario (Fig. 4c). Spatially, under the SSP126 scenario, DSL increased in the central and eastern parts of the study region (Fig. 4d). Under the other scenarios, DSL was reduced over most areas (Fig. 4e–g), DSO was significantly delayed in all regions and DSE changed significantly in a few areas (Supplementary Fig. 16). However, in southern Sumatra, the future DSL is projected to have an upward trend, implying a heightened fire risk in the future. This analysis suggests that the future DSL change depends on the emission scenarios, with a continuing decrease under medium- and high-emission scenarios. Considering the strong influence of DSL on fire activities, future fire carbon emissions will likely be further suppressed by increasing precipitation and reductions in DSL in the future.

For future changes in precipitation under different emission scenarios in EQAS, anthropogenic aerosols and GHG remain the main driving factors[32]. We utilized the SSP 245-nat, SSP 245-aer, and SSP 245-GHG experiments from the MIROC6 model' DAMIP simulations (the reason for model selection can be found in the "Methods" section) to simulate precipitation in EQAS from 2023–2099 and analyzed the separate responses of precipitation
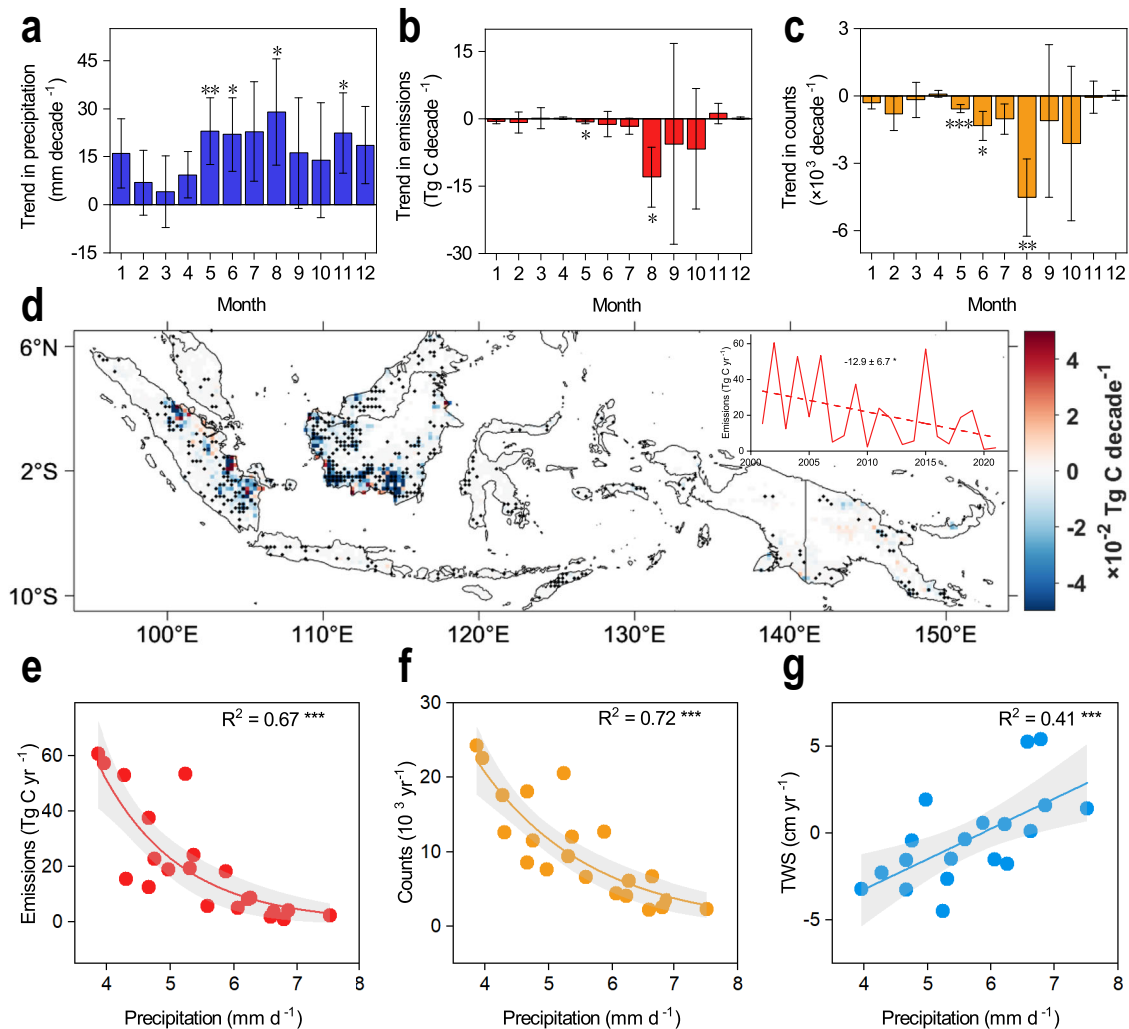
Fig. 3 Fire-related changes in EQAS, 2001–2021. a–c, Monthly trends in precipitation (**a**), fire carbon emissions (**b**), and fire counts (**c**). Error bars indicate the standard error of linear trends. **d** Spatial trends in fire carbon emissions in August 2001–2021. Only grid points with annual mean fire carbon emissions >0.001 Tg C for 2001–2021 are shown. Black dots indicate grids with a significant linear trend ($p < 0.1$). The inset shows the annual average fire carbon emissions and their linear trend in August. The numbers show the linear trend (Tg C decade^{-1}) and standard error of fire carbon emissions. **e–g** Exponential fitting of precipitation for May–August to fire carbon emissions (**e**) and fire counts (**f**) in August. Linear fitting of precipitation for May–August to terrestrial water storage (TWS) (**g**) in August. The TWS is for the period 2003–2021. The coefficient of determination (R^2) are shown in the top right corners. Shading indicates 95% confidence intervals. *$p < 0.1$; **$p < 0.05$; ***$p < 0.01$.

to anthropogenic aerosols and GHG (Supplementary Table 3). As shown in Supplementary Fig. 17, similar to the results in the historical period (Supplementary Fig. 5), GHG emissions have a promoting effect on precipitation in EQAS, while anthropogenic aerosol emissions have an inhibitory effect on precipitation in EQAS. Previous study[32] has indicated that by 2100, as anthropogenic aerosol emissions decrease, GHG emissions will dominate the differences between different SSPs. This is also the primary reason for precipitation and dry season length changes in EQAS.

In summary, this study indicates a negative trend in DSL over EQAS due to increased precipitation in the past decades, contrasting with the positive DSL trend over the Amazon and Congo rainforests[11,12]. This change in DSL (-34.4 ± 18.6 d decade^{-1}) was further found to reduce the FSL (-22.8 ± 10.0 d decade^{-1}) and lead to reduced fire carbon emissions (May: -0.7 ± 0.4 Tg C decade^{-1}; August: -12.9 ± 6.7 Tg C decade^{-1}), highlighting the role of increasing precipitation in controlling fire carbon emissions. The fire risk is likely to be further suppressed by the continued increase of precipitation and associated reductions in DSL in the future. These findings provide a scientific reference

for fire management practices in EQAS. Tropical peatlands play an important role in the global carbon cycle[33], and EQAS has the largest peatlands in the tropics[3], underscoring the importance of studying the impact of changes in DSL in the region on fire.

METHODS
Study area

In this study, we focused on the relationship between dry seasons and fire carbon emissions from 2001 to 2021 in EQAS, with this region being selected according to the regional divisions of the Global Fire Emissions Database[34]. According to Climatic Research Unit (CRU)[35] climate data and CPC-U precipitation, the mean annual EQAS precipitation is almost 2500 mm, and the mean annual mean temperature is 26 °C. Most fire carbon emissions in the region arise from the burning of peatlands[36] caused by human deforestation activities, on the edges of forest fragmentation, and during agricultural land clearance[37]. "Slash-and-burn" is a common method of agricultural land clearance that leads to a large
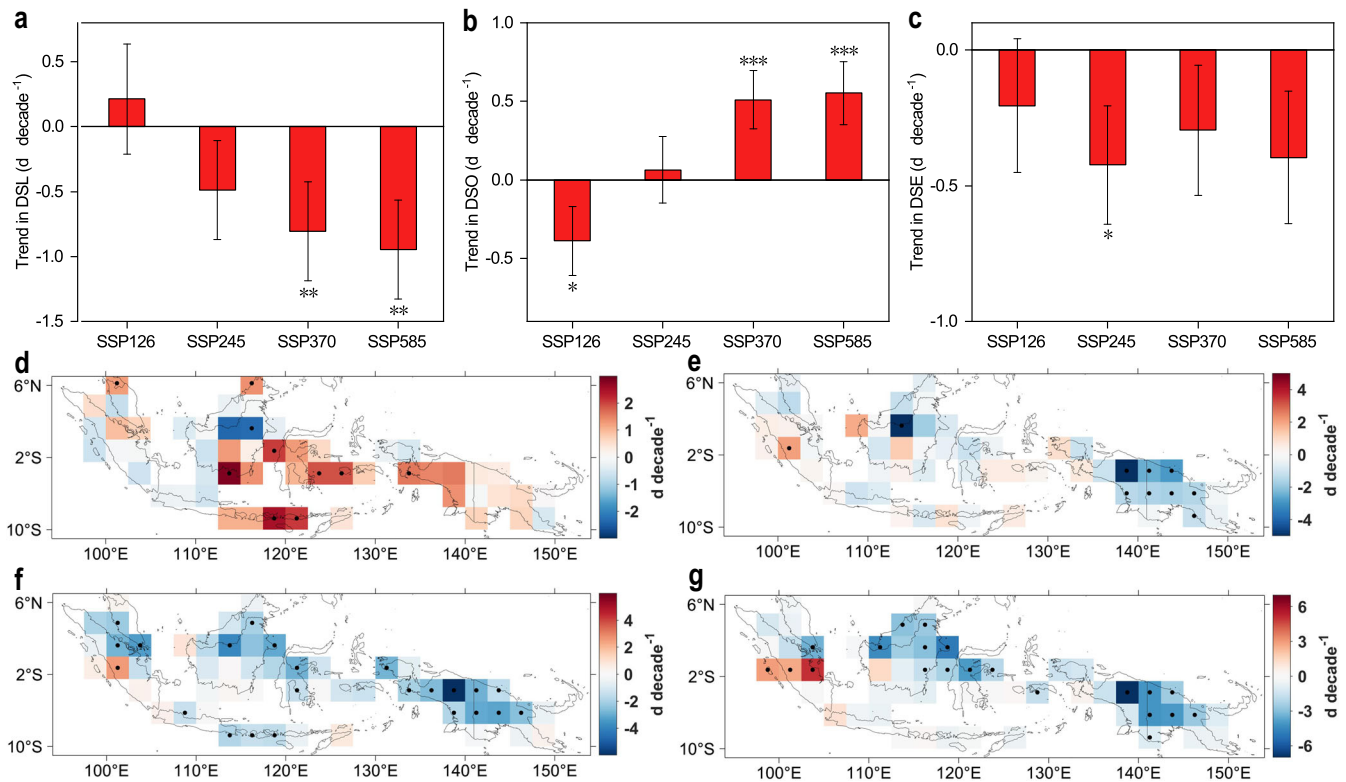
Fig. 4 Future dry season trends under different scenarios, and spatial patterns of future linear DSL trends. a–c Multi-model averaged trends in DSL (**a**), DSO (**b**), and DSE (**c**) calculated using 12 selected CMIP6 models for 2023–2099 under the SSP126, SSP245, SSP370, and SSP585 scenarios. Error bars indicate the standard error of linear trends. **d–g** Multi-model averaged trends in DSL calculated using the 12 CMIP6 models for 2023–2099 under the SSP126 (**d**), SSP245 (**e**), SSP370 (**f**), and SSP585 (**g**) scenarios. Black dots indicate grids with significant linear trends ($p < 0.1$). *$p < 0.1$; **$p < 0.05$; ***$p < 0.01$.

number of out-of-control fires being lit during the dry season[38], in which 89.0% of the EQAS fire carbon emissions are concentrated.

Two main fire regions were selected for analysis: southern Sumatra (6°S–0°, 99°–106°E) and southern–central Kalimantan (4°S–0°, 110°–117°E), consistent with previous studies[14] (Supplementary Fig. 1). Their dry season fire carbon emissions accounted for 27.2% (southern Sumatra) and 43.7% (south-central Kalimantan) of the total dry season EQAS emissions, respectively.

Climate data

To examine dry season changes in EQAS, three widely used precipitation datasets were collected to achieve more robust results (Supplementary Table 4). We used observational gridded daily rainfall data from the CPC-U[19] at 0.5° × 0.5° resolution for the period 1979–2021 and 5-day data from the GPCP[21] at 2.5° × 2.5° resolution for the period 1979–2016. CPC-U and GPCP precipitation data are combinations of gauge and satellite observations. A daily precipitation product from the ERA5[20] reanalysis with a horizontal resolution of about 31 km was regridded to a 0.25° × 0.25° resolution for the period 1979–2021 were also used.

GRACE data

We used monthly GRACE products (2003–2021) with a resolution of 0.5° × 0.5° to monitor changes in TWS in EQAS. GRACE Mascon solutions (Release 06 (RL06) v2) generated by the National Aeronautics and Space Administration Jet Propulsion Laboratory (JPL)[39] and the Center for Space Research (CSR)[40] at the University of Texas, respectively, were used. The means of the two products were used for analysis. Records missing for several months were replaced by averaged values from nearby months.

Fire data

For fire data, we used satellite-derived biomass-burning carbon emissions data from the Global Fire Emissions Database Version 4.1 (GFED4s) at 0.25° × 0.25° resolution. This dataset provides bottom-up estimates of global fire carbon emissions since 1997[17,41]. Zheng et al.[30] provided estimates of global monthly fire carbon emissions for 2000–2021 at a horizontal resolution of 3.75° × 1.9°, using carbonic oxide (CO) inversion from the Measurements of Pollution in the Troposphere (MOPITT) satellite and the global atmospheric inversion system. Fire counts data were obtained from the MOD14A2 (Version 006)[16] product collected by the Terra satellite with a spatial resolution of 1 km and a temporal resolution of 8 days from 2001 to 2021. Monthly fire counts are calculated by averaging the 8-day fire counts (divided by eight) and adding them up to a monthly value.

In EQAS, severe fires emit much smoke haze per unit area, usually causing a decrease in atmospheric visibility. Therefore, airport visibility data can be used as a long-term proxy for fire emissions[14]. Daily visibility records were obtained from the National Oceanic and Atmospheric Administration Integrated Surface Database. Visibility records involved three surface stations at southern Sumatra airports and three at southern–central Kalimantan airports (Supplementary Fig. 1; Supplementary Table 5). As there is a large data gap during 1989–1991, we selected records for 1992–2021 for analysis. We calculated daily visibility data as B_{ext} by using the empirical Kosch-Mieder relationship for 1992–2021, with reports of zero visibility being replaced with 0.1 km[9]. B_{ext} is used to indicate the degree to which visible light is attenuated with distance due to aerosol absorption and scattering.

Future precipitation data

Future daily precipitation data were obtained from CMIP6 simulations. We selected 20 models with daily precipitation simulations for 1979–2014 (Supplementary Table 3). We used projections of future precipitation and dry season changes under four scenarios, SSP126, SSP245, SSP370, and SSP585, representing low- to high-emissions scenarios. Compared with CMIP5, the new scenarios in CMIP6 are based on shared socioeconomic pathways (SSPs) and work in harmony with Representative Concentration Pathways (RCPs) through shared policy assumptions[42].

We utilized the hist-nat, hist-aer, and hist-GHG experiments from the CMIP6 models' DAMIP simulations[25] to analyzed the separate responses of historical precipitation to anthropogenic aerosols and GHG, attributing observed changes in historical precipitation to natural, GHG, and anthropogenic aerosol emissions (Supplementary Table 3). In order to improve the robustness of our results, we selected 4 (MIROC6, MRI-ESM2-0, FGOALS-g3, IPSL-CM6A-LR) from the 12 models that can reproduce the DSL shortening over the historical period. We also utilized the SSP 245-nat, SSP 245-aer, and SSP 245-GHG experiments from the MIROC6 and NorESM2-LM models' DAMIP simulations to analyzed the separate responses of historical precipitation to anthropogenic aerosols and GHG, attributing observed changes in future precipitation to natural, GHG, and anthropogenic aerosol emissions (Supplementary Table 3) and only the MIROC6 model reflects DSL shortening during the historical period among these two models (Supplementary Fig. 14). All precipitation simulations were resampled at $2.5° \times 2.5°$ resolution before being analyzed.

Defining dry and fire seasons

DSO and DSE were defined as the days corresponding to the maximum and minimum days of the cumulative precipitation anomaly each year, respectively. The DSL in each grid box was calculated from the difference between DSO and DSE. This method had been used previously for the examination of dry season changes over the Congo and Amazon rainforest areas[43,44]. We used a harmonic analysis to determine whether each grid box experienced one or more dry seasons per year. When the amplitude of the second or third harmonic was greater than or equal to the amplitude of the first harmonic, multiple dry seasons were involved. Double dry seasons in EQAS occurred mainly in northern Sumatra, and only the second dry season (near the mean dry season date of EQAS) was selected for analysis. The specific calculation process involved the relationship

$$S(d) = \sum_{i=t_0}^{d} (P_i - \overline{P})
\tag{1}$$

where P_i is the rainfall on day i; i ranged from t_0 to the day (d) being considered; t_0 is the date when the harmonic analysis was used to calculate the minimum of the first harmonic in the annual mean precipitation cycle of each grid point, which ensures that the correct dry season is captured; and $\overline{P}$ is the mean rainfall rate for all days of all years in mm day^{-1}. $S(d)$ was calculated for each day from t_0 to d and smoothed using a 1–2–1 filter passed 50 times. The inflection point, S, marks the onset and end of the dry season[45].

We also calculated the fire season using Eq. (1) with the 8-day fire counts and daily B_{ext}. Using the 8-day fire counts to calculate the fire season, where P_i is the fire counts on 8-day i; i ranged from t_0 to the day (d) being considered, t_0 is the first day of the calendar year, and the day (d) is the last day of the calendar year; $\overline{P}$ is the mean fire counts for all 8-days of all years; $S(d)$ was calculated for each 8-day from t_0 to d. Using daily B_{ext} to calculate the fire season, where P_i is the B_{ext} on day i; i ranged from t_0 to the day (d) being considered, t_0 is the first day of the calendar year, and the day (d) is the last day of the calendar year; $\overline{P}$ is the mean fire

counts for all days of all years; $S(d)$ was calculated for each day from t_0 to d. The inflection point, S, marks the onset and end of the fire season. There may be multiple fire seasons in some low-fire years, in which case we chose the longest fire season between May and October as that year's fire season.

Inflection point analysis of variables

Piecewise regression[46] was applied in detecting inflection points in the trends of variables, as follows:

$$y = \begin{cases} \beta_0 + \beta_1 t + \varepsilon, t \leq \alpha \\ \beta_0 + \beta_1 t + \beta_2(t - \alpha) + \varepsilon, t > \alpha \end{cases}
\tag{2}$$

where y is the tested variable, t is the year, α is the year of trend change, β_0 is the y intercept, β_1 is the linear trend when t is less than or equal to α, $\beta_1 + \beta_2$ is the linear trend when t is greater than α, and ε is the residual of the fit. Least-squares linear regression was used to test the significance of trends, with the statistical significance level (p) being assessed by a two-tailed Student's t-test, and with $p < 0.1$ considered significant.

Long-term trend analysis

Least-squares methods were used to evaluate the linear trends of the studied variables. Its statistical significance level (p) was assessed by the two-tailed Student's t-test to verify.

Correlation analysis

The linear correlation coefficient (Pearson's R) was calculated between variables to quantify their concurrent and lagged association. The significance of the correlation, p, was assessed using a two-tailed Student's t-test.

Data uncertainties

Due to the bottom-up nature of satellite-based fire detection, the detection of small fires can be hindered by smoke and cloud cover[29]. In addition, the detection capabilities are limited by the resolution of satellite sensors. These issues have resulted in both MODIS and GFED4.1s based on MODIS fire products are considered to be blind to small fires, particularly the small, smoldering fires related to agricultural activities[47]. In addition, emissions from small fires in GFED4.1s are heavily parameterized[28]. We calculated the proportion of fire carbon emissions generated by small fires from 2001 to 2016 in relation to the total fire carbon emissions. The results show that fire carbon emissions from small fires account for ~20% of the total fire carbon emissions (Supplementary Fig. 18). This may affect the trend changes of fire carbon emissions in EQAS.

To improve the robustness of our results and reduce the uncertainty in estimating small fire emissions based on MODIS fire products, we conducted top-down estimations of fire carbon emissions in EQAS using the MOPITT CO observations and atmospheric inversions. Due to the spatial heterogeneity and short atmospheric lifetime of CO distribution in the atmosphere, as well as advancements in atmospheric inversion techniques, there is potential for using satellite-based CO monitoring to estimate fire carbon emissions[30]. Our results indicate that in EQAS, the monthly estimated fire CO_2 emissions using CO inversion and the estimated fire carbon emissions using GFED4s are highly consistent (Supplementary Fig. 18a). Both top-down and bottom-up estimates of fire carbon emissions show a significant decrease in May and August in EQAS (Supplementary Fig. 18b, c). This analysis further confirmed the decreasing trend of fire carbon emissions in EQAS.

DATA AVAILABILITY

CODE AVAILABILITY

REFERENCES

1. Saatchi, S. S. et al. Benchmark map of forest carbon stocks in tropical regions across three continents. *Proc. Natl Acad. Sci. USA* **108**, 9899–9904 (2011).
2. Werf, G. R. V. D., Dempewolf, J., Trigg, S. N., Randerson, J. T. & Defries, R. S. *Proc. Natl Acad. Sci. USA* **105**, 20350–20355 (2009).
3. Page, S. E., Rieley, J. O. & Banks, C. J. Global and regional importance of the tropical peatland carbon pool. *Glob. Change Biol.* **17**, 798–818 (2011).
4. Page, S. E. et al. The amount of carbon released from peat and forest fires in Indonesia during 1997. *Nature* **420**, 61–65 (2002).
5. Chen, Y. et al. A pan-tropical cascade of fire driven by El Niño/Southern Oscillation. *Nat. Clim. Change* **7**, 906–911 (2017).
6. Pan, X., Chin, M., Ichoku, C. M. & Field, R. D. Connecting Indonesian fires and drought with the type of El Niño and phase of the Indian Ocean dipole during 1979–2016. *J. Geophys. Res. Atmos.* **123**, 7974–7988 (2018).
7. Huang, X. et al. Smoke-weather interaction affects extreme wildfires in diverse coastal regions. *Science* **379**, 457–461 (2023).
8. Hendon, H. H. Indonesian rainfall variability: impacts of ENSO and local air–sea interaction. *J. Clim.* **16**, 1775–1790 (2003).
9. Murphy, K. The ENSO-fire dynamic in insular Southeast Asia. *Clim. Change* **74**, 435–455 (2006).
10. Field, R. D., Van Der Werf, G. R. & Shen, S. S. Human amplification of drought-induced biomass burning in Indonesia since 1960. *Nat. Geosci.* **2**, 185–188 (2009).
11. Fu, R. et al. Increased dry-season length over southern Amazonia in recent decades and its implication for future climate projection. *Proc. Natl Acad. Sci. USA* **110**, 18110–18115 (2013).
12. Jiang, Y. et al. Widespread increase of boreal summer dry season length over the Congo rainforest. *Nat. Clim. Change* **9**, 617–622 (2019).
13. Xu, H. et al. Rising ecosystem water demand exacerbates the lengthening of tropical dry seasons. *Nat. Commun.* **13**, 1–11 (2022).
14. Field, R. D. et al. Indonesian fire activity and smoke pollution in 2015 show persistent nonlinear sensitivity to El Niño-induced drought. *Proc. Natl Acad. Sci. USA* **113**, 9204–9209 (2016).
15. Yin, Y. et al. Variability of fire carbon emissions in equatorial Asia and its nonlinear sensitivity to El Nio. *Geophys. Res. Lett.* **43**, 10472–10479 (2016).
16. Giglio, L., Schroeder, W. & Justice, C. O. The collection 6 MODIS active fire detection algorithm and fire products. *Remote Sens. Environ.* **178**, 31–41 (2016).
17. Van Der Werf, G. R. et al. Global fire emissions estimates during 1997–2016. *Earth Syst. Sci. Data* **9**, 697–720 (2017).
18. Eyring, V. et al. Overview of the Coupled Model Intercomparison Project Phase 6 (CMIP6) experimental design and organization. *Geosci. Model Dev.* **9**, 1937–1958 (2016).
19. Chen, M. et al. Assessing objective techniques for gauge-based analyses of global daily precipitation. *J. Geophys. Res. Atmos.* **113**, D04110 (2008).
20. Hersbach, H. et al. The ERA5 global reanalysis. *Q. J. R. Meteorol. Soc.* **146**, 1999–2049 (2020).
21. Xie, P. et al. GPCP pentad precipitation analyses: an experimental dataset based on gauge observations and satellite estimates. *J. Clim.* **16**, 2197–2214 (2003).
22. Dayem, K. E., Noone, D. C. & Molnar, P. Tropical western Pacific warm pool and maritime continent precipitation rates and their contrasting relationships with the Walker Circulation. *J. Geophys. Res. Atmos.* **112**, D06101 (2007).
23. Seager, R. et al. Strengthening tropical Pacific zonal sea surface temperature gradient consistent with rising greenhouse gases. *Nat. Clim. Change* **9**, 517–522 (2019).
24. Ma, S. & Zhou, T. Robust strengthening and westward shift of the tropical Pacific Walker circulation during 1979–2012: A comparison of 7 sets of reanalysis data and 26 CMIP5 models. *J. Clim.* **29**, 3097–3118 (2016).
25. Gillett, N. P. et al. The detection and attribution model intercomparison project (DAMIP v1. 0) contribution to CMIP6. *Geosci. Model Dev.* **9**, 3685–3697 (2016).
26. Ayantika, D. et al. Understanding the combined effects of global warming and anthropogenic aerosol forcing on the South Asian monsoon. *Clim. Dyn.* **56**, 1643–1662 (2021).
27. Putra, E. I. The effect of the precipitation pattern of the dry season on peat fire occurrence in the Mega Rice Project area, Central Kalimantan, Indonesia. *Tropics* **19**, 145–156 (2011).
28. Randerson, J., Chen, Y., Van Der Werf, G., Rogers, B. & Morton, D. Global burned area and biomass burning emissions from small fires. *J. Geophys. Res. Biogeosci.* **117**, G04012 (2012).
29. Giglio, L., Van der Werf, G., Randerson, J., Collatz, G. & Kasibhatla, P. Global estimation of burned area using MODIS active fire observations. *Atmos. Chem. Phys.* **6**, 957–974 (2006).
30. Zheng, B. et al. Record-high CO2 emissions from boreal fires in 2021. *Science* **379**, 912–917 (2023).
31. Field, R. D. & Shen, S. S. Predictability of carbon emissions from biomass burning in Indonesia from 1997 to 2006. *J. Geophys. Res. Biogeosci.* **113**, G04024 (2008).
32. Wilcox, L. J. et al. Accelerated increases in global and Asian summer monsoon precipitation from future aerosol reductions. *Atmos. Chem. Phys.* **20**, 11955–11977 (2020).
33. Ribeiro, K. et al. Tropical peatlands and their contribution to the global carbon cycle and climate change. *Glob. Change Biol.* **27**, 489–505 (2021).
34. van der Werf, G. R. et al. Interannual variability in global biomass burning emissions from 1997 to 2004. *Atmos. Chem. Phys.* **6**, 3423–3441 (2006).
35. Harris, I., Osborn, T. J., Jones, P. & Lister, D. Version 4 of the CRU TS monthly high-resolution gridded multivariate climate dataset. *Sci. Data* **7**, 1–18 (2020).
36. Xu, J., Morris, P. J., Liu, J. & Holden, J. PEATMAP: refining estimates of global peatland distribution based on a meta-analysis. *Catena* **160**, 134–140 (2018).
37. Jones, M. W. et al. Global and regional trends and drivers of fire under climate change. *Rev. Geophys.* **60**, 1–76 (2022).
38. Ketterings, Q. M., Wibowo, T. T., Van Noordwijk, M. & Penot, E. Farmers' perspectives on slash-and-burn as a land clearing method for small-scale rubber producers in Sepunggur, Jambi Province, Sumatra, Indonesia. *For. Ecol. Manag.* **120**, 157–169 (1999).
39. Landerer, F. W. & Swenson, S. Accuracy of scaled GRACE terrestrial water storage estimates. *Water Resour. Res.* **48**, W04531 (2012).
40. Watkins, M. M., Wiese, D. N., Yuan, D. N., Boening, C. & Landerer, F. W. Improved methods for observing Earth's time variable mass distribution with GRACE using spherical cap mascons. *J. Geophys. Res. Solid Earth* **120**, 2648–2671 (2015).
41. Giglio, L., Randerson, J. T. & Van Der Werf, G. R. Analysis of daily, monthly, and annual burned area using the fourth-generation global fire emissions database (GFED4). *J. Geophys. Res. Biogeosci.* **118**, 317–328 (2013).
42. O'Neill, B. C. et al. The scenario model intercomparison project (ScenarioMIP) for CMIP6. *Geosci. Model Dev.* **9**, 3461–3482 (2016).
43. Liebmann, B. & Marengo, J. Interannual variability of the rainy season and rainfall in the Brazilian Amazon Basin. *J. Clim.* **14**, 4308–4318 (2001).
44. Dunning, C. M., Black, E. C. & Allan, R. P. The onset and cessation of seasonal rainfall over Africa. *J. Geophys. Res. Atmos.* **121**, 11405–411,424 (2016).
45. Bombardi, R. J., Kinter, J. L. III & Frauenfeld, O. W. A global gridded dataset of the characteristics of the rainy and dry seasons. *Bull. Am. Meteorol. Soc.* **100**, 1315–1328 (2019).
46. Toms, J. D. & Lesperance, M. L. Piecewise regression: a tool for identifying ecological thresholds. *Ecology* **84**, 2034–2041 (2003).
47. Zhang, T., Wooster, M. J., De Jong, M. C. & Xu, W. How well does the 'small fire boost'methodology used within the GFED4. 1s fire emissions database represent the timing, location and magnitude of agricultural burning? *Remote Sens.* **10**, 823 (2018).

AUTHOR CONTRIBUTIONS

B.H. designed the study. S.F.W. performed analysis. B.H. and S.F.W. drafted the paper. H.W.C., D.L.C., Y.N.C., W.P.Y., F.S., J.P.D., W.W., T.X.C., L.L.G., Z.Q.Z., W.L.D., Z.Li, W.G.J., L.H., X.M.H., R.T., H.M.L., Y.F.Z., and X.M.X. improved the study.

COMPETING INTERESTS

The authors declare no competing interests.

ADDITIONAL INFORMATION

Supplementary information The online version contains supplementary material available at https://doi.org/10.1038/s41612-023-00455-7.

Correspondence and requests for materials should be addressed to Bin He.

Reprints and permission information is available at http://www.nature.com/reprints

Publisher's note Springer Nature remains neutral with regard to jurisdictional claims in published maps and institutional affiliations.